ORNL/TM-2024/3464

Complete Optimization of Laser Powder Bed Fusion Nickel-Based Alloys Downselected from FY 2023 Candidate Materials Including Thermodynamic Modeling, Sample Fabrication, and Microstructure Characterization

Sebastien Dryepondt
et al.

July 2024

M3CT-24OR1304042

ORNL IS MANAGED BY UT-BATTELLE LLC FOR THE US DEPARTMENT OF ENERGY

DOCUMENT AVAILABILITY

Reports produced after January 1, 1996, are generally available free via OSTI.GOV.

Website www.osti.gov

Reports produced before January 1, 1996, may be purchased by members of the public from the following source:

National Technical Information Service
5285 Port Royal Road
Springfield, VA 22161
Telephone 703-605-6000 (1-800-553-6847)
TDD 703-487-4639
Fax 703-605-6900
E-mail info@ntis.gov
Website http://classic.ntis.gov/

Reports are available to US Department of Energy (DOE) employees, DOE contractors, Energy Technology Data Exchange representatives, and International Nuclear Information System representatives from the following source:

Office of Scientific and Technical Information
PO Box 62
Oak Ridge, TN 37831
Telephone 865-576-8401
Fax 865-576-5728
E-mail reports@osti.gov
Website https://www.osti.gov/

This report was prepared as an account of work sponsored by an agency of the United States Government. Neither the United States Government nor any agency thereof, nor any of their employees, makes any warranty, express or implied, or assumes any legal liability or responsibility for the accuracy, completeness, or usefulness of any information, apparatus, product, or process disclosed, or represents that its use would not infringe privately owned rights. Reference herein to any specific commercial product, process, or service by trade name, trademark, manufacturer, or otherwise, does not necessarily constitute or imply its endorsement, recommendation, or favoring by the United States Government or any agency thereof. The views and opinions of authors expressed herein do not necessarily state or reflect those of the United States Government or any agency thereof.

ORNL/TM-2024/3464

Advanced Materials and Manufacturing Technologies

COMPLETE OPTIMIZATION OF LASER POWDER BED FUSION NICKEL-BASED ALLOYS DOWNSELECTED FROM FY 2023 CANDIDATE MATERIALS INCLUDING THERMODYNAMIC MODELING, SAMPLE FABRICATION, AND MICROSTRUCTURE CHARACTERIZATION

Sebastien Dryepondt
Stephen Taller
Zakary Snow
Holden Hyer
Amir Ziabari
Yi-Feng Su

July 2024

M3CT-24OR1304042

Prepared by
OAK RIDGE NATIONAL LABORATORY
Oak Ridge, TN 37831
managed by
UT-BATTELLE LLC
for the
US DEPARTMENT OF ENERGY
under contract DE-AC05-00OR22725

CONTENTS

LIST OF FIGURES

LIST OF TABLES

ABBREVIATIONS

AM	additive manufacturing
AMMT	Advanced Materials and Manufacturing Technologies
BD	build direction
EBSD	electron backscatter diffraction
EDS	energy-dispersive x-ray spectroscopy
INL	Idaho National Laboratory
LPBF	laser powder bed fusion
NE	Office of Nuclear Energy
ORNL	Oak Ridge National Laboratory
SEM	scanning electron microscopy
STEM	scanning transmission electron microscopy
XCT	x-ray computed tomography

ACKNOWLEDGMENTS

The authors would like to thank K. Carver, J. Moser, B. Abbott, D. Newberry, and T. Lowe for their help with the experimental work and acknowledge M. Ridley and A. Heimbrook for carefully reviewing the manuscript. This research was funded by the US Department of Energy Office of Nuclear Energy's Advanced Materials and Manufacturing Technologies program.

ABSTRACT

The goal of the Advanced Materials and Manufacturing Technologies (AMMT) program is to accelerate the incorporation of new materials and manufacturing technologies into advanced nuclear-related systems. Although 316H stainless steel fabricated by laser powder bed fusion (LPBF) has already been identified as an alloy that could have a significant effect on various reactor technologies, many other materials and manufacturing techniques are being evaluated. Nickel-based alloys typically offer higher-temperature capabilities compared with advanced stainless steels, and previous reports looked at three Ni-based alloy categories: low-Co alloys with a potential use close to the reactor core; high-temperature, high-strength alloys; and molten salt–compatible alloys. In the first category, alloy 718 was studied in 2023, and creep testing at 600°C and 650°C revealed that the alloy exhibited great creep strength after the appropriate annealing but had low ductility. Advanced characterization was recently conducted to highlight the presence of strengthening γ' and γ'' precipitates after creep testing and to show that brittle phases at grain boundaries might explain the low ductility of LPBF 718 compared with wrought 718. For the high-temperature, high-strength alloys, previously purchased powders of alloys 617, 230, and 625 were used to assess the printability of these three solution-strengthened alloys. Hot cracking could not be suppressed for alloy 617 and 230, and it was shown that these cracks, which were elongated along the build direction (BD), had a drastic effect on the ductility of alloy 230 at room temperature when specimens were machined perpendicular to the BD. On the contrary, LPBF printing of crack-free alloy 625 was achieved using similar printing parameters, and the alloy looked like a promising candidate for various reactor technologies. The fabrication of alloy 282 by LPBF, a γ'-strengthened alloy with great creep strength up to 800°C, was performed in 2023, and x-ray computed tomography (XCT) scans of the alloy before and after creep testing at 750°C were carried out to assess the effect of flaws on the alloy's creep behavior. Correlation between the flaws' volume fraction, creep ductility, and creep lifetime could be established, and future work on LPBF 625 will take full advantage of in situ printing data and ex situ XCT scans to accelerate the alloy qualification. Finally, single track experiments were performed on the two alloys previously identified as good molten salt–resistant, Ni-based candidates: Hastelloy N and 244. Various laser parameters were considered, and cracking was not observed for either of the two alloys. Wrought 244 offers better creep strength and molten salt compatibility than alloy 625, and future work will aim to establish the alloy LPBF processing window.

1. INTRODUCTION

Additive manufacturing (AM) offers the ability to fabricate complex, near net shape components, reducing the need for machining, welding, or brazing during postprocessing [1]. Additionally, the US Department of Energy Office of Nuclear Energy's (NE's) Transformational Challenge Reactor program [2] demonstrated the first rapid component qualification paradigm using a combination of sensor outputs from visible-light images and health monitoring streams collected in situ during the LPBF printing, as well as machine learning to create an advanced diagnostic tool [3–4]. The AMMT program [5] is focused on the pursuit of rapid qualification of new materials processed by advanced manufacturing technologies for current and advanced nuclear reactors. The core effort of the AMMT program has been focused on stainless steel 316H fabricated by AM, and several reports have already highlighted how digital manufacturing, rapid material characterization and testing, and microstructure and properties modeling could accelerate the deployment of AM 316H [5–6]. Other classes of alloys and manufacturing techniques are of interest for various reactor components, and a decision criteria matrix was established collectively by Oak Ridge National Laboratory (ORNL), Idaho National Laboratory (INL), Pacific Northwest National Laboratory, and Argonne National Laboratory to select materials based on their relative importance among the candidate nuclear materials and their AM technological readiness [8]. ORNL and INL investigated Ni-based alloys considering the following three categories.

1. Low-Co alloys—This category focuses on alloys that could be used close to the reactor core, including alloy 800H, alloy 718, and alloy 625. Although 800H was the only code-qualified alloy, the lack of data on 800H produced by AM and the difficulty in procuring 800H powder resulted in a low scorecard for the alloy, and no further work was considered under the AMMT program. Alloys 625 and 718 are well-known to the AM community and are already in use in nuclear reactors in the wrought condition [9]. They are being considered for applications in advanced reactors. Work on alloy 718 was initiated in FY 2023 using legacy material from the Transformational Challenge Reactor program [10–11] and was continued in FY 2024. Because of its potential for higher-temperature applications, work on 625 was initiated in FY 2024 and will be discussed in this report.

2. High-temperature, high-strength alloys—These alloys can potentially operate at temperatures >700°C. Alloy 617 is a key alloy in this category as the only code-qualified Ni-based alloy for use in the pressure vessel [12]. Studies on the fabrication of 617 by AM are scarce [13, 14], and the production of 617 by LPBF will be discussed based on the authors' initial printability study. Alloy 617 is compared in this report with alloy 230 [15], another solution-strengthened alloy considered for various high-temperature applications because of its good balance of strength and oxidation resistance at high temperature. Although few studies have been published on 230 fabricated by AM [16–18], the powder was readily available, allowing direct comparison of these two alloys fabricated by LPBF. LPBF 625 was used as a reference solution-strengthened alloy with excellent printability that is already in use in various high-temperature applications. In addition to solution-strengthened alloys, a very high-strength γ'-strengthened alloy, Haynes 282, was printed and creep tested. Although several other high-strength, high-temperature alloys have been discussed in a previous report, including alloys specifically designed for AM [19], alloy 282 was selected because of the powder availability and increasing interest in the alloy for AM applications [20].

3. Low-Cr alloys—These alloys are compatible with fluoride and chloride molten salts for operating temperature superior to ~700°C. Two alloys were identified: Hastelloy N, an ORNL alloy specifically designed for molten salt applications [21], and alloy 244, a high-strength alloy originally designed for parts requiring low thermal expansion but with a Cr content of only 8 wt % [22].

This report is focused on the printability and performance of these Ni-based alloys. Techno-economic considerations will be discussed in a subsequent report on Ni-based alloys fabricated by LPBF and directed energy deposition prepared in collaboration with INL.

2. LOW-COBALT 718 ALLOY

2.1 PREVIOUS RESULTS ON LPBF 718

Alloy 718 is the most popular Ni-based alloy and has a broad range of applications in the aerospace and gas turbine industries, which were early adopters of AM. The alloy is already in use in nuclear reactor cores or primary coolant circuits in various reactors [9]. Extensive discussion on the fabrication and performance of LPBF alloy 718 can be found elsewhere [8, 23]. The previous report focused on the creep properties of alloy 718 [8], concluding that the LPBF 718 alloy exhibited similar creep strength as wrought 718 after annealing according to the following heat treatment: homogenization at 1,174°C for 2 h and 1,204°C for 6 h, and then solution annealing at 1,093°C for 1 h and aging at 718°C and 621°C, both for 8 h [11]. The as-printed LPBF 718 exhibited slightly lower creep strength both along and perpendicular to the BD, and low ductility was observed for both the annealed and as-printed materials. In

FY 2024, work was focused on advanced microstructure characterization to elucidate the high strength and low ductility of the LPBF 718 alloy. A summary of the experimental procedure for fabrication and creep testing of the LPBF 718 is given in the following paragraph, and additional information can be found elsewhere [8, 10].

Fabrication of a large block of alloy 718 was performed on a Concept Laser X-Line 2000R using the following printing parameters: laser power of 370 W, spot size of 0.3 mm, scanning speed of 500 mm/s, hatch spacing of 0.16 mm, and scan rotation between layers of 67°. The powder chemistry, given by the powder manufacturer, was as follows: Ni–18.22Fe–18.99Cr–5.15Nb–3Mo–0.93Ti–0.5Al–0.1Co–0.04Si–0.04C–0.012N–0.016O (wt %). Creep testing was conducted on 25.4 mm long SS3-type dog bone specimens with gage dimensions of 7.62 × 2 × 1 mm. Specimens were machined along and perpendicular to the BD for the as-printed LPBF 718 and only along the BD for the annealed material. Creep testing was conducted on dead-load frames, and specimens were heated using a radiation furnace. Two thermocouples were attached to the specimens, and a 30 min hold at temperature ensured a temperature gradient of less than 4°C before starting the test. The applied stresses were 650 or 750 MPa at 600°C and 600 or 650 MPa at 650°C. Rods clamped to the top and bottom grips were connected to two linear variable differential transformers to measure specimen deformation.

2.2 MICROSTRUCTURE CHARACTERIZATION

2.2.1 As-Fabricated Microstructure

Scanning electron microscopy (SEM) was performed on a Tescan Mira3 equipped with Si drift energy dispersive x-ray spectroscopy (EDS) and an EDAX Velocity Plus electron backscatter diffraction (EBSD) camera. AZtec software was used to index the Kikuchi band structure and determine the lattice Euler angles, and the open-source MTEX toolbox (processed in MATLAB 2023) was employed to generate orientation maps and inverse pole figures. A Hitachi focused ion beam operated at 40 kV was used to fabricate specimens for scanning transmission electron microscopy (STEM). STEM-EDS characterization was then conducted on an FEI Talos FX20 operated at 200 kV and equipped with an extreme field emission gun electron source as well as a Super-XEDS system with four Si drift detectors.

EBSD orientation maps showing the grain structure of the as-printed and annealed 718 can be found in [8]. Elongated grains along the BD were observed for the as-printed LPBF 718 with an average equivalent grain diameter of 8.3 ± 0.22 µm. After annealing, recrystallization resulted in an equiaxed grain structure with an average grain size of 37.9 ± 2.6 µm. An elongated cellular structure has been previously observed by SEM and STEM for the as-printed material with the presence of both the Laves phase and δ phase in the cell walls [8, 10]. Higher STEM magnification also revealed the presence of both γ' and γ'' precipitates [10].

As shown in Figure 1, additional STEM characterization was conducted on the as-printed material in an area close to the gage section of one of the creep-tested specimens. The presence of a cellular structure with a high density of dislocations within the cells was confirmed, but neither γ' nor γ'' were observed. The likely explanation is local variation in cooling rates during printing, leading to significant changes in precipitate formation.

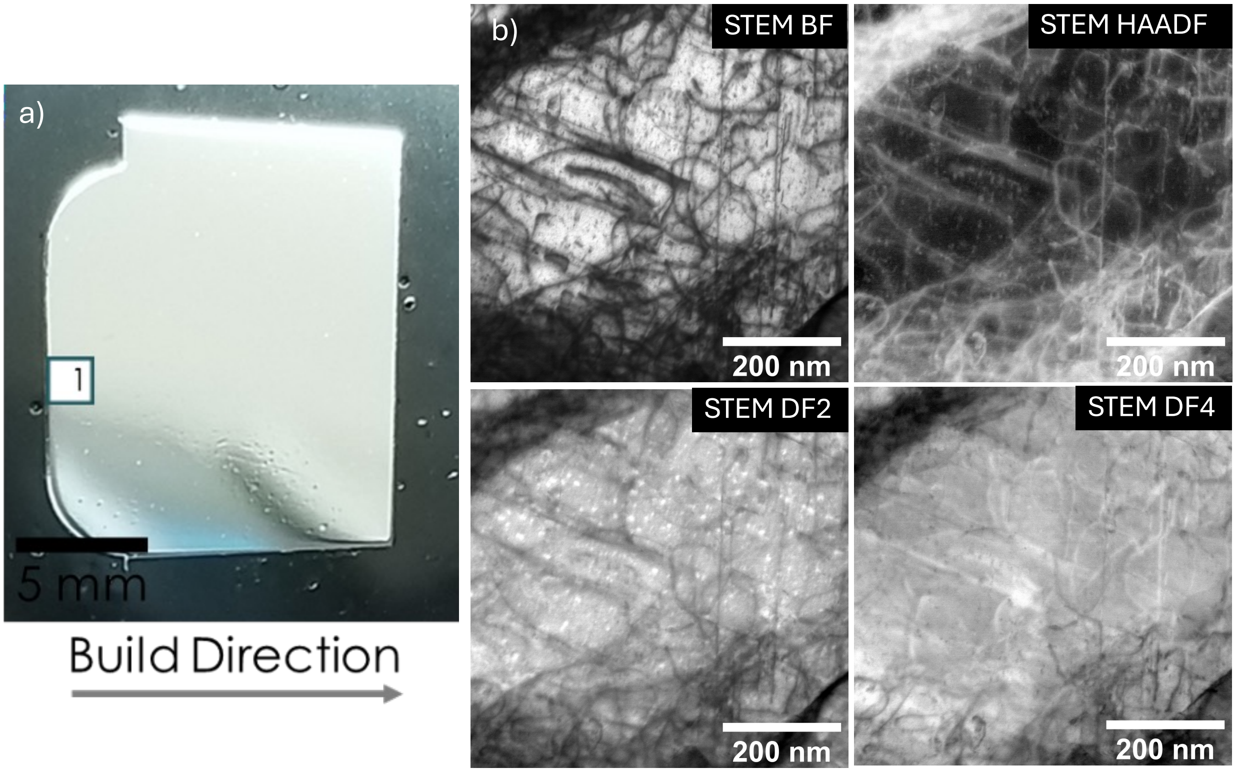

Figure 1. a) Lift-out for STEM characterization taken from an area close to the specimen gage area, and b) STEM micrographs highlighting the presence of a high dislocation density but no γ′ or γ″ precipitates. Rectangle 1 in a) indicates where the STEM images were acquired.

2.2.2 LPBF 718 Microstructure After Creep Testing As-Fabricated Specimen

The SEM micrograph shown in Figure 2a of the creep specimen tested at 650°C and 650 MPa highlights the presence of cracks at grain boundaries consistent with the observed intergranular fracture. The initial cellular structure was still observed after creep testing with a high density of precipitates in the cell walls, as shown in Figure 2b. The higher STEM micrograph and associated chemical maps, shown in Figure 3, revealed Cr-rich precipitates, which were likely oxides, (Nb,Ti)-rich carbides, and (Nb,Mo)-rich precipitates that were likely Laves phases. A few (Ni,Nb)-rich precipitates, not present in Figure 3, were also observed locally in the cell wall of the creep tested specimen. These observations are very consistent with the precipitates reported by Taller et al. in the cell walls of the as-printed alloy [10]. These brittle precipitates were also observed at grain boundaries, which likely played a role in the alloy's low ductility at rupture.

The chemical maps in Figure 3 also highlight the presence of a very fine dispersion of nano-size, (Nb,Ti)-rich γ′ and γ″ precipitates. These precipitates formed either after printing or during creep testing at 650°C and are the likely explanation for the great creep strength of the as-printed LPBF 718.

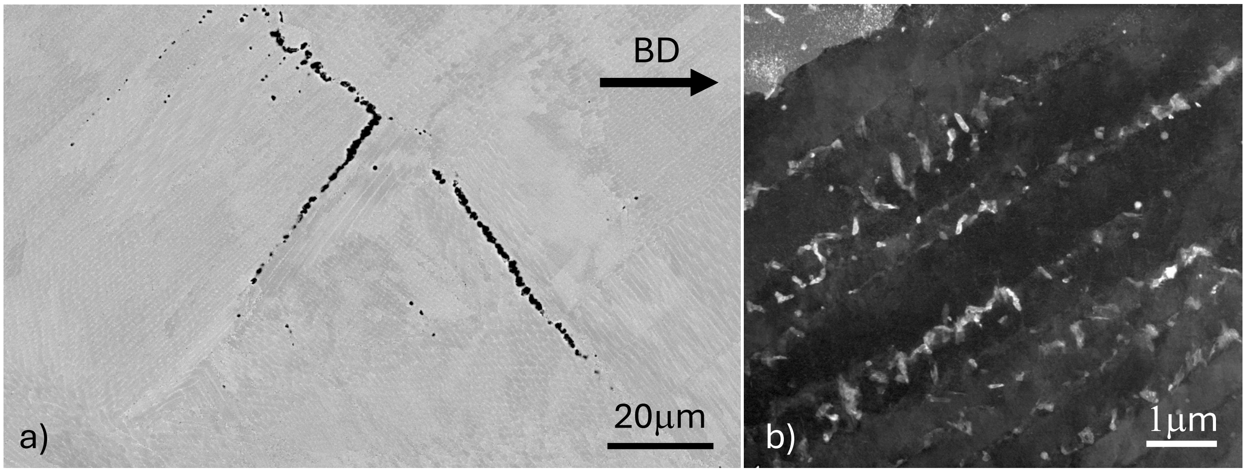

Figure 2. Specimen creep tested at 650°C with an applied stress of 650 MPa for 384 h. (a) SEM micrograph showing precipitates in the cell walls and at grain boundaries and cracking at grain boundaries. (b) STEM micrograph highlighting a high density of precipitates within the cell walls.

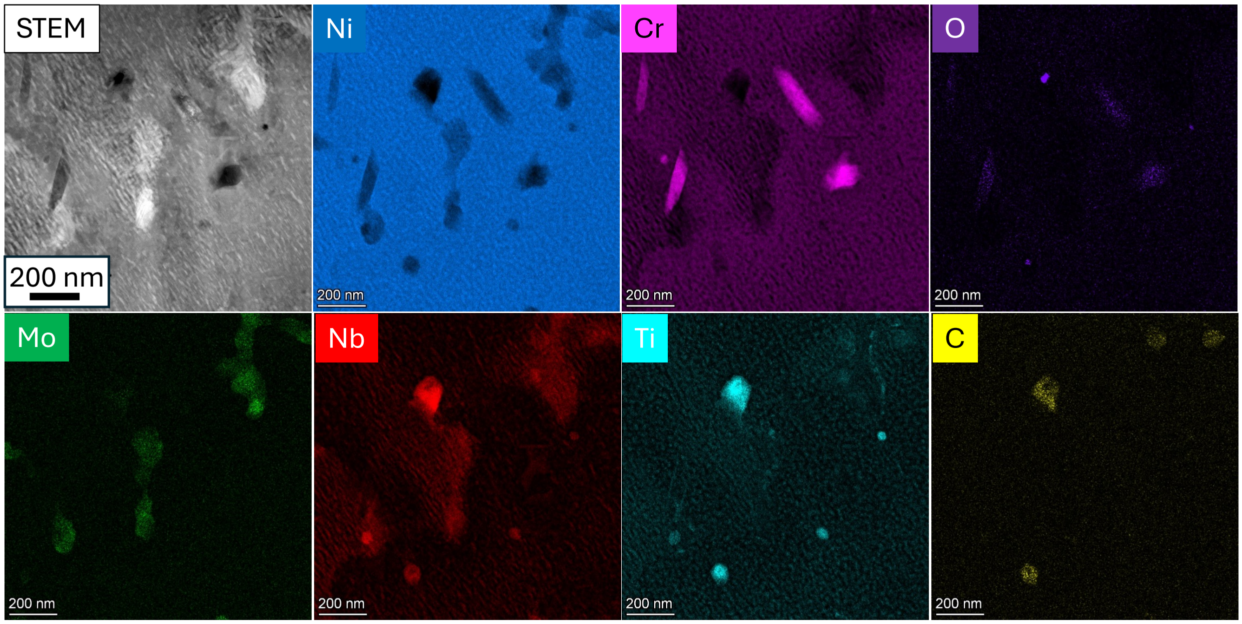

Figure 3. Specimen creep tested at 650°C with an applied stress of 650 MPa for 384 h: STEM micrograph and corresponding elemental maps.

2.2.3 LPBF 718 Microstructure After Creep Testing, Annealed Specimen

SEM micrographs of the annealed specimen creep tested at 650°C and 650 MPa are presented in Figure 4. A few large precipitates and cracks were observed at grain boundaries, leading to an intergranular fracture. These large precipitates were identified by EDS as brittle (Nb,Ti)-rich carbides [8]. The STEM micrograph and corresponding EDS maps shown in Figure 5 revealed the presence of a high density of nano precipitates with two distinct populations: very fine precipitates 10–30 nm in size and elongated precipitates ~150 nm in length. The high concentration of Ni and low concentration of Al indicate that the elongated precipitates are likely γ'', and the smaller precipitates are likely γ'. Again, the presence of these strengthening precipitates is likely the reason for the high strength of the annealed LPBF 718 alloy.

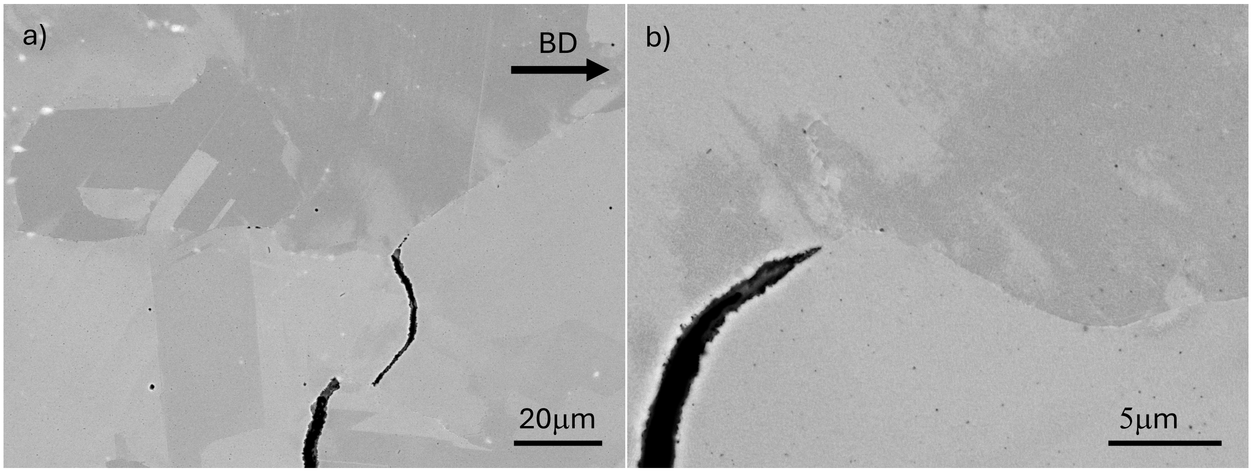

Figure 4. SEM micrographs of the annealed specimen creep tested at 650°C with an applied stress of 650 MPa, highlighting the presence of precipitates and cracks at grain boundaries.

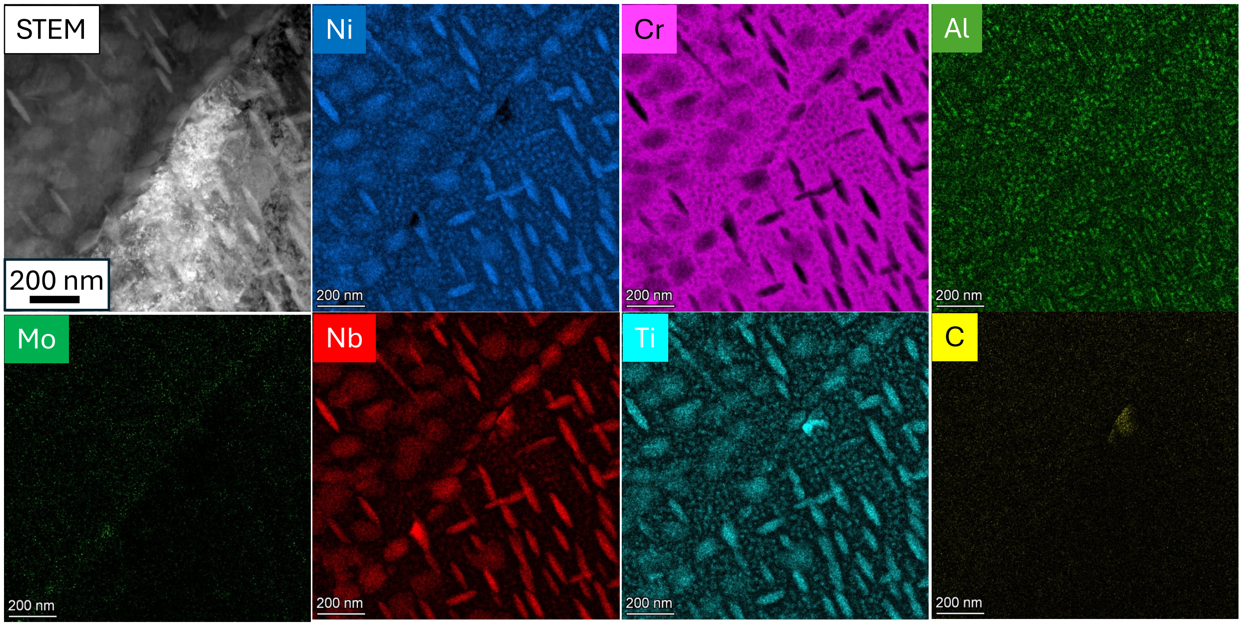

Figure 5. Transmission electron micrograph of the annealed specimen creep tested at 650°C with an applied stress of 650 MPa, showing a high density of γ' and γ'' nano precipitates and precipitates at grain boundaries.

2.3 CONCLUSION ON LPBF 718

This work has shown that with the appropriate heat treatment, LPBF 718 offers similar creep strength as wrought 718 [8]. The heat treatment needs to be performed at higher temperature compared with wrought 718 to remove the chemical segregation in the cell structure because of rapid cooling during LPBF fabrication [10]. Even in the as-printed conditions, acceptable creep strength was measured consistent with the presence of nano γ' and γ'' precipitates. Local thermal history during printing may or may not result in the formation of these precipitates, but in situ aging and precipitate formation will take place during creep testing at 600°C–650°C. Although 718 is an outstanding alloy at intermediate temperature, the lack of stability of the γ'' phase imposes an upper temperature limit of approximately 650°C [24]. Although several studies have considered the use of LPBF 718 at higher temperatures [19], this is mainly related to the alloy availability and printability rather than the alloy performance at $T > 650$°C. As discussed later in this report, alloy 625 offers better mechanical and oxidation properties at $T > 650°C$ compared with alloy 718 and, as such, might be considered for a broader range of NE applications.

3. HIGH-TEMPERATURE, HIGH-STRENGTH ALLOYS

3.1 SOLUTION-STRENGTHENED ALLOYS 617, 230, AND 625

The creep strength of the wrought 617, 230, and 625 alloys were compared in the Larson–Miller plot in Figure 6 with creep data for wrought 230 and 625 from Haynes International [15, 25] and data for alloy 617 from [12]. The Larson–Miller Parameter (*LMP*) was calculated according to the relation in Equation (1):

$$LMP = T(\mathrm{K}) * \left(C + \log\left(t_r(h)\right)\right), \text{with } C = 20, \tag{1}$$

with T equal to the temperature in Kelvin and t_r equal to time to rupture in hour.

Although the creep strength of alloys 230 and 617 were similar, the creep strength of alloy 625 was lower at low stress and high temperature, but the latter can easily be printed by LPBF.

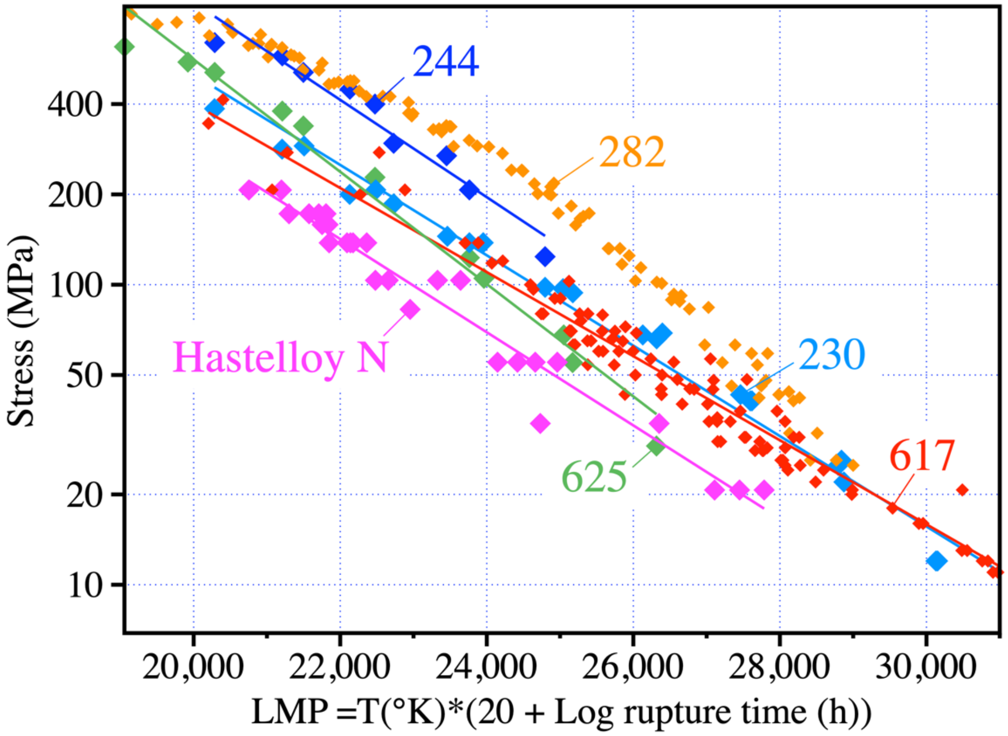

Figure 6. Larson–Miller plot comparing the creep resistance of five wrought Ni-based alloys [12, 15, 21, 22, 25, 32].

3.1.1 LPBF Parameter Optimization for Alloys 230, 617, and 625

A Renishaw AM250, fitted with a reduced build volume to limit powder consumption, was used to print the 230, 617, and 625 alloys, and the powder chemistries provided by the powder manufacturers are given in Table 1. Small cubes with dimensions of 5 × 10 × 12 mm were initially fabricated to explore a broad range of printing conditions, and the parameter ranges are given in Table 2. For each condition, the energy density (*ED*) was calculated according to Equation (2):

$$ED = \frac{P}{\frac{p}{t \times dt} \times h \times l} \left(\frac{\mathrm{J}}{\mathrm{mm}^3}\right), \tag{2}$$

where *P* is the laser power, *p* the point distance, *t* the laser dwell time, *dt* is the delay time of the laser between pulses, *h* the hatch spacing, and *l* the layer thickness. After removal from the build plate, the density of the cubes was measured using the Archimedes method, and the cube's relative density with respect to the energy density is shown in Figure 7a. All the LPBF-processed alloys showed a very similar trend with a rapid increase of the relative density with increasing energy density up to 91 J/mm^3 followed by a plateau with a relative density of 98.7% for alloy 230, 99.3% for alloy 617, and 99.3% for alloy 625. As shown in Figure 7b, increasing the energy density above 91 J/mm^3 had an effect on the alloy grain structure with the disappearance of small grain areas and the exclusive presence of elongated grains along the BD for the cube fabricated with the higher energy density.

Although a high alloy density could be achieved for the three LPBF alloys, cracking could not be suppressed for alloys 230 and 617, with a higher crack density for the LPBF 230 [26]. Figure 8 shows that many cracks were aligned with the BD and the grain structure. These cracks are likely due to hot tearing, and their presence has been discussed extensively for another solution-strengthened Ni-based alloy fabricated by LPBF—Hastelloy X (Ni–22Cr–18.5Fe–9Mo–2Co) [27–29]. The high residual stress caused by rapid cooling and thermal cycling during printing was determined to be a key factor for crack formation. The role of the alloy strength at very high temperature, microsegregation, and carbide formation have been discussed, which led to the conclusion that precise chemistry control, composition modification, or nanoparticle addition would be needed for the formation of crack-free LPBF Hastelloy X [30]. Zhao et al. added Zr in alloy 230 and showed that the alloy could be produced crack-free [17]. Thermodynamic calculations were initiated to assess the effect of chemistry modification on the printability of alloy 617.

Table 1. Powder chemistries (wt %) for the 617, 230, and 625 alloys provided by the powder manufacturers

Alloy	Ni	Cr	Mo	W	Co	Fe	Nb	Mn	Si	Ti	Al	C	O	N	B	Other
617	Bal.	22	9	—	12	—	—	—	—	—	1	0.05	0.01	0.01	—	—
230	Bal.	21	2	13	1	1	<0.5	0.6	0.4	<0.1	0.3	0.1	—	—	0.002	0.02La
625	Bal.	21.5	8.89	—	0.05	4.19	3.66	0.01	—	—	0.06	0.02	0.017	0.015	—	—

Table 2. Parameters explored during printing of the three alloys

	Power (W)	**Point Distance (µm)**	**Dwell Time (µs)**	**Hatch Spacing (µm)**	**Layer Thickness (µm)**	**Delay Time (µs)**
Range	150–350	55–110	60–180	60–120	60	10
Selected 91.7 J/mm^3	350	70	100	100	60	10
Selected 195 J/mm^3	250	40	140	80	60	10

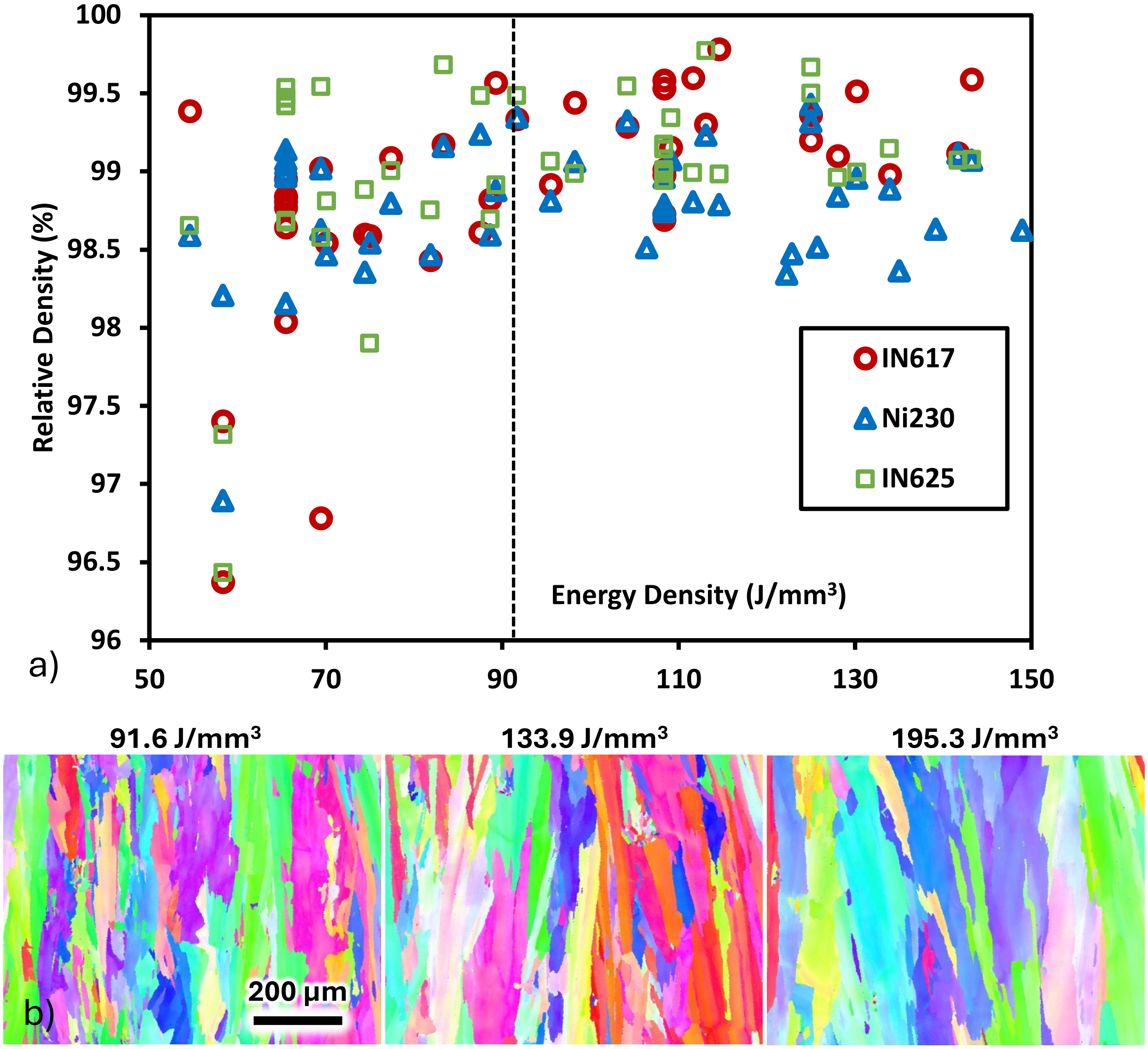

Figure 7. (a) Relative density measured using the Archimedes method versus printing energy density for LPBF 617, 230, and 625. (b) EBSD orientation maps highlighting the effect of the energy density on the grain morphology for LPBF 230.

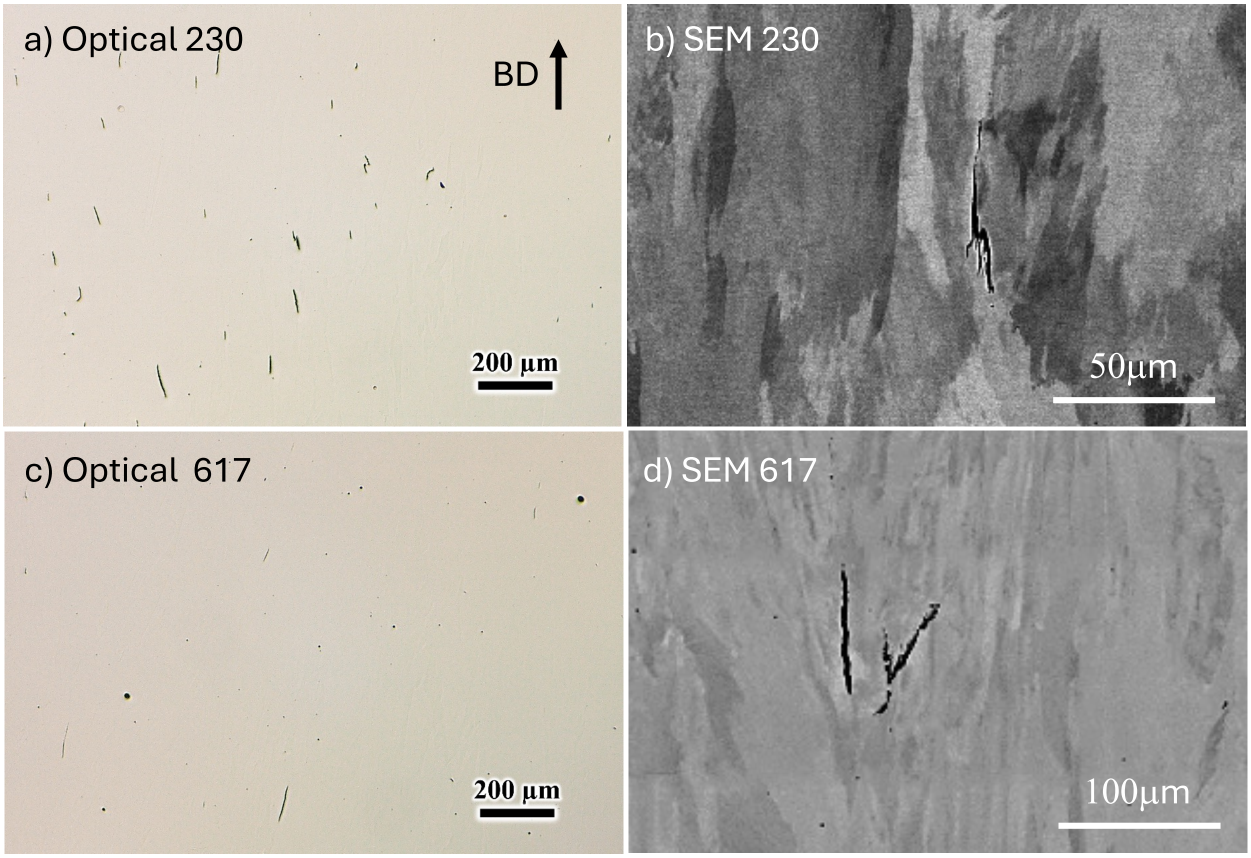

Figure 8. Micrographs of the LPBF 230 and 617 alloys showing the presence of cracks: (a) 230 optical, (b) 230 SEM, (c) 617 optical, and (d) 617 SEM.

3.1.2 Tensile Testing of Alloy 230

Two sets of printing parameters, detailed in Table 2, with corresponding energy densities of 91.7 J/mm^3 and 195 J/mm^3, respectively, were selected for the fabrication of 25.4 × 25.4 ×12.7 mm blocks, allowing the machining of small dog bone specimens with a gage length of 7.62 mm and a gage section of 2 × 2 mm. Specimens were machined along and perpendicular to the BD, and tensile curves at room temperature are given in Figure 9a, with the properties summarized in Table 3. Excellent tensile properties were observed for the 91.7 J/mm^3 specimens machined along the BD, with average yield strength, ultimate tensile strength, and plastic deformation of 590 MPa, 869 MPa, and 50%, respectively. These values are similar to the values expected for wrought 230 plates [15] except for a yield strength of only 383 MPa for wrought 230. High yield strengths are frequently observed for LPBF alloys because of the high dislocation density in the cell walls. Slightly lower yield strength and ultimate tensile strength were measured for the 195 J/mm^3 specimens, and further characterization is needed to evaluate the role of the grain and cell structures. A drastic decrease in ductility and moderate decrease in ultimate tensile strength were observed for the specimens machined perpendicular to the BD. The optical micrographs displayed in Figure 9b highlight the critical role played by the cracks in the alloy oriented perpendicular to the BD.

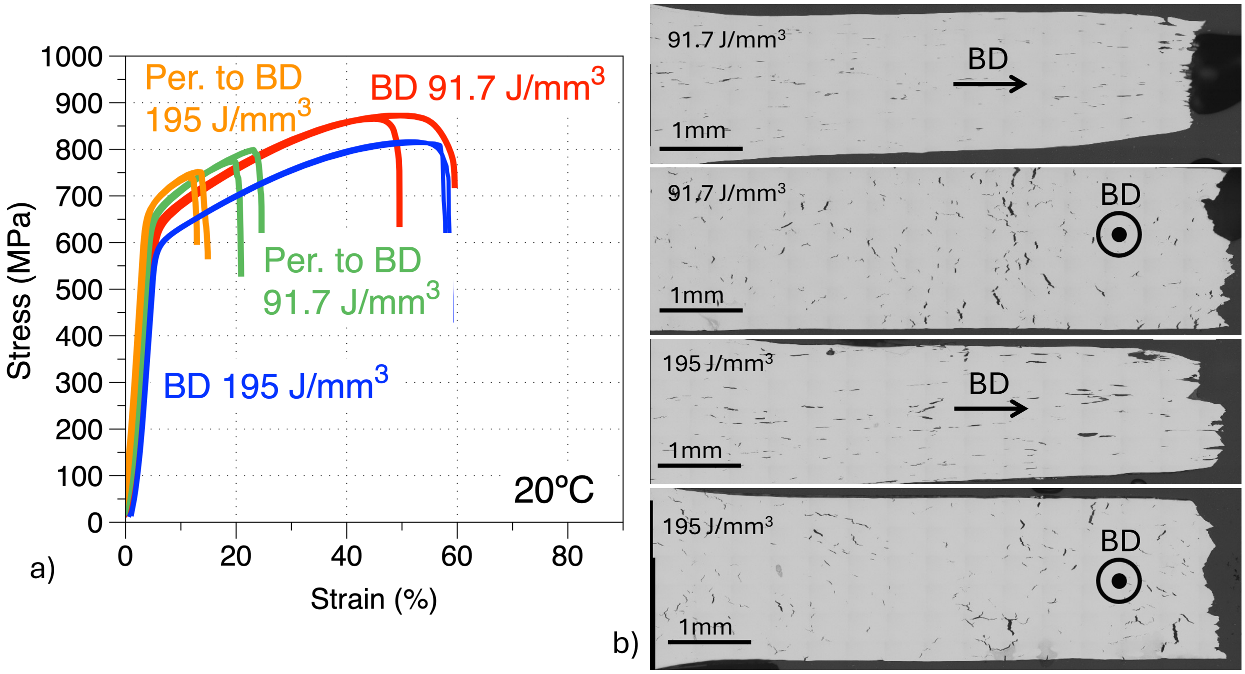

Figure 9. (a) Tensile curves at room temperature for LPBF 230 along and perpendicular to the BD. (b) Cross-sectional micrographs of the specimens after tensile testing.

Table 3. LPBF 230 tensile properties at room temperature

Energy Density	Orientation	Yield Strength (MPa)	Ultimate Tensile Strength (MPa)	Plastic Strain (%)
91.7 J/mm^3	Perpendicular to BD	618.8	798.6	20.9
91.7 J/mm^3	Perpendicular to BD	621.4	774.8	17.9
91.7 J/mm^3	BD	588.6	873.0	54.8
91.7 J/mm^3	BD	592.7	865.9	45.4
195 J/mm^3	Perpendicular to BD	636.6	740.8	9.8
195 J/mm^3	Perpendicular to BD	637.2	751.7	11.8
195 J/mm^3	BD	560.8	817.4	56.5
195 J/mm^3	BD	559.4	813.7	54.8

3.2 γ′-STRENGTHENED 282 ALLOY

3.2.1 LPBF 282 Material Characterization

The fabrication of alloy 282 by LPBF using a Renishaw AM250 has been described in previous work [8]. Six 101 mm long vertical rods were used to machine 89 mm long creep specimens with a 6.35 mm gage section in diameter and 31.75 mm in length. The specimens were annealed according to the heat treatment recommended by INL [8]: 1 h at 1,180°C followed by 4 h at 800°C. This heat treatment resulted in only a partial recrystallization of the alloy with a bimodal distribution and numerous small grains, resulting in an average equivalent diameter of approximately 13 ± 13µm.

The leftover material from each rod was cross-sectioned for microstructure characterization, and optical micrographs of the C5 and T5 rods after the full heat treatment are shown in Figure 10. The density of flaws was significantly higher for the C5 specimen compared with the T5 specimen. In fact, all the rods from the left of the build exhibited a high flaw density (C1, C3, and C5) compared with the rods from the right of the build (T1, T3, and T5).

To correlate in situ printing data with the resulting LPBF 282 microstructure, images generated during printing were analyzed. As shown in Figure 10e, spatter particles were observed more frequently for the C1 to C5 rods compared with the T1 to T5 rods, which might explain the variation in flaw density.

Further nondestructive analysis was conducted using an Industrial ZEISS Metrotom XCT system equipped with a 200 kV source. Radiographic images of the gage section of the creep specimens were captured from various angles and used to algorithmically reconstruct 3D representations of these specimens. For all XCT scans, a short-scan strategy with 145 views between 0° and 197° was employed, and each view was an average of 8 × 1 s acquisition. Reconstruction was performed for XCT scans acquired before and after creep testing using advanced deep learning–based algorithms [31].

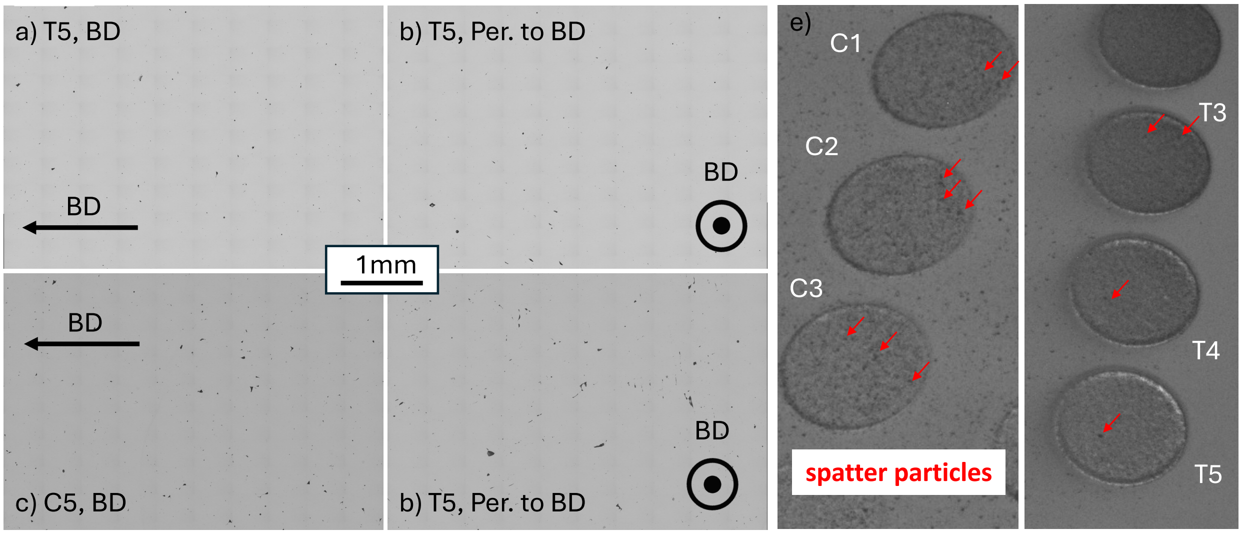

Figure 10. (a)–(d) Optical micrographs of the LPBF282 alloy after heat treatment: (a) T5 specimen along the BD, (b) T5 specimen perpendicular to the BD, (c) C5 specimen along the BD, and (d) C5 specimen perpendicular to the BD. (e) In situ images acquired during printing.

3.2.2 LPBF 282 Creep Results

Creep testing was conducted at 750°C with an applied stress of 300 MPa or 350 MPa using lever arm machines according to ASTM Standard E139 [32]. Thermocouples were attached to the gage section, and the temperature was maintained at 750°C ± 3°C. Rods clamped to the specimen heads were connected to linear variable differential transformers to measure specimen deformation. The creep curves presented in Figure 11a revealed similar secondary creep rates but lower ductility and slightly lower lifetimes for the C1 and C3 specimens compared with the T1 and T3 specimens. The C5 and T5 specimens were interrupted for XCT scan analysis before rupture. Figure 11b shows that the creep strength of the LPBF 282 was only slightly lower than the creep strength of wrought 282, but the strain at rupture for the LPBF 282 specimens was quite low; as the wrought 282 ductility was expected to be >20% at 750°C [33].

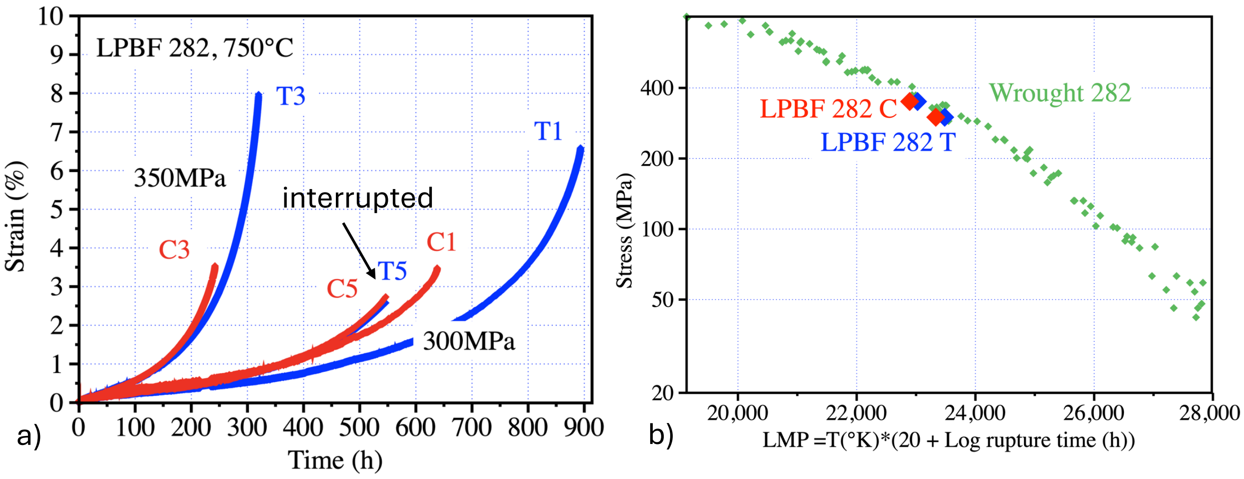

Figure 11. (a) LPBF 282 creep curve generated at 750°C with an applied stress of 300 MPa or 350 MPa. (b) Larson–Miller plot comparing the creep strength of the LPBF 282 with the creep properties of wrought 282.

3.2.3 Microstructure Analysis of the LPBF 282 Creep Specimens

The 3D reconstructions shown in Figure 12a and Figure 12b from the XCT scans of the C3 and T3 specimens before and after testing confirmed the significantly higher volume fraction of flaws in the C3 specimen compared with the T3. Additionally, an increase in flaws after testing was obvious for both the C3 and T3 specimens. The volume fractions of flaws before and after testing were estimated from the XCT scans and are given in Figure 12c. In addition to the expected difference between the C and T specimens, significant variation was also observed between the C1, C3, and C5 specimens. An increase in flaws after creep testing was confirmed for all the LPBF 282 specimens. Additional analysis of the flaw distribution in the specimens before and after testing is given in Figure 13.

For the T1, T3, and T5 specimens, a significant increase of the number of flaws less than 250 µm in size was observed after creep testing. These new flaws are likely related to creep cavitation, and cross-sectional microstructure characterization will be performed to determine if these flaws are related to specific microstructural features. An increase in size of a few very large flaws was observed for T1 and T3, tested to rupture, but not for the interrupted T5 specimen. These flaws are likely playing a key role in the final rupture stage of the specimens and might partly explain the LPBF 282 alloy's low ductility.

The initial number of flaws less than 250 µm in size was drastically higher for the C1 and C3 specimens in comparison with the T1 and T3 specimens (Figure 13). A further increase of these 250 µm or less flaws was observed after creep testing for the C3 specimen and to a lesser extent for the C1 specimen. For the later specimen, creep testing resulted, however, in a drastic increase of the number of flaws more than 250 µm in size. Ongoing work is aiming at the registration of each initial flaw for all the specimens to determine the flaw evolution during creep testing and determine which flaws are affecting specimen failure.

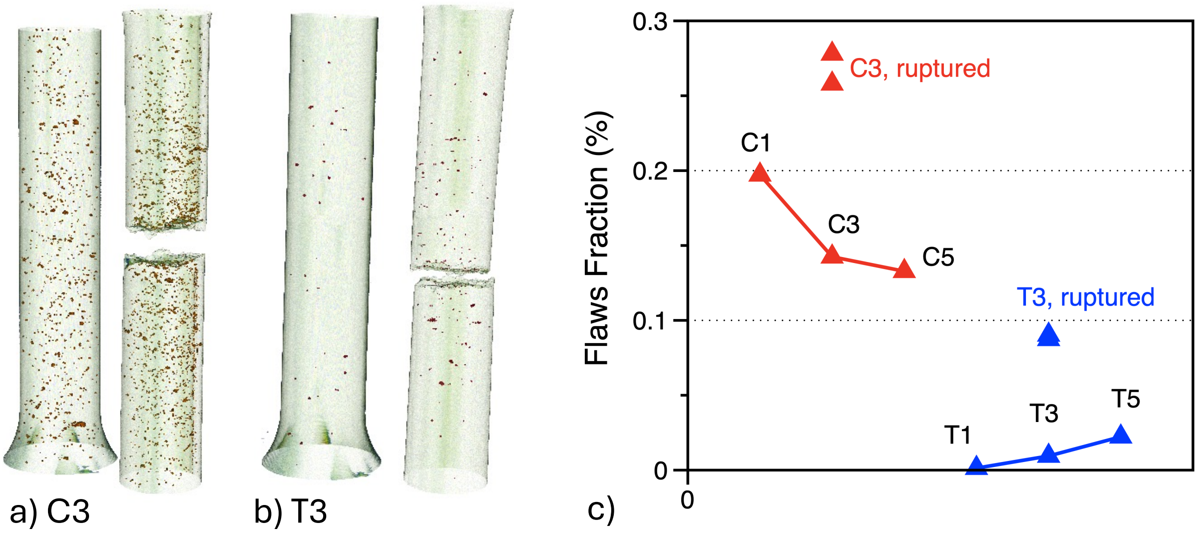

Figure 12. 3D reconstruction of the (a) C3 and (b) T3 specimens before and after creep testing. (c) Volume fraction of flaws in the C and T specimens before and after creep testing.

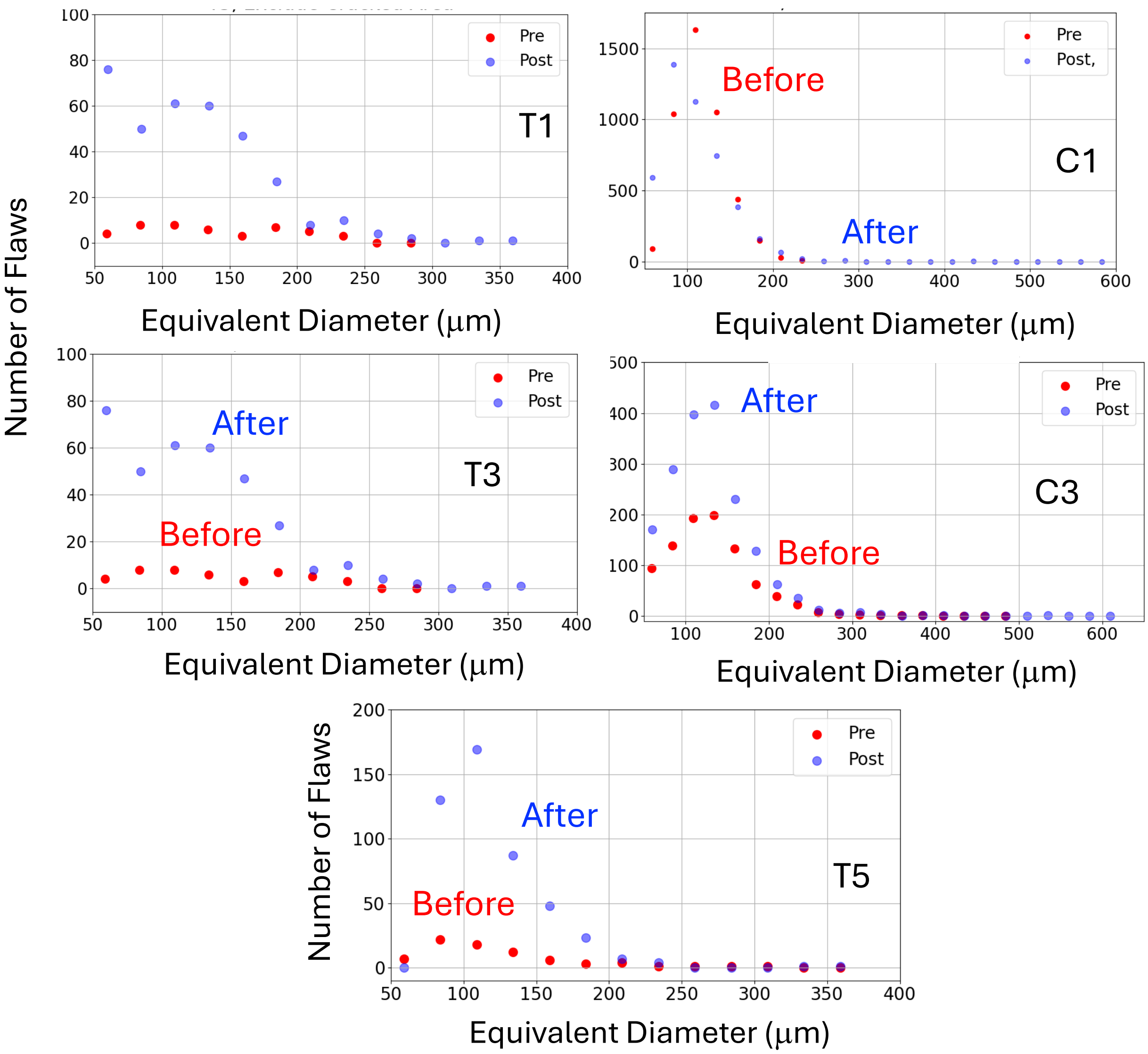

Figure 13. Number of flaws versus equivalent diameter for all the LPBF 282 specimens before and after creep testing. The rupture area was removed because a flaw's size was difficult to evaluate.

3.3 CONCLUSION ON HIGH-TEMPERATURE, HIGH-STRENGTH ALLOYS

Both the 617 and 230 alloys exhibited limited printability, and significant work would be required to produce these alloys by LPBF crack-free. Modification of the alloys' chemistries would likely be needed and would necessitate the purchase of custom-made powders. On the other hand, powder for alloy 625 is readily available and relatively affordable, and the 625 alloy offers a wide LPBF printing parameter window.

Additionally, although the creep properties of alloy 625 above 700°C are inferior to the properties of the 617 and 230 alloys, the strength of the alloy at a high temperature is significantly better than the strength of alloy 316H. The compatibility of the alloy with molten salt is inferior to the low-Cr Ni-based alloys that will be discussed later but is again superior to the compatibility of alloy 316H. As will be discussed in a subsequent report, the overall high-temperature properties of alloy 625 make the alloy attractive to a broad range of nuclear reactors, and LPBF 625 will be the focus of this project in FY 2025. Alloy 282 is also a compelling alloy because of its superior creep strength and powder availability. Although the alloy is known to be printable because of the relatively low Ti and Al content [34], these results highlight the need for a careful printing strategy to avoid flaws in the final build that could affect the alloy ductility. This work has also demonstrated that the use of in situ data and XCT scans can provide crucial information to establish correlation between the printed microstructure and the LPBF 282 creep properties. Such an approach is at the center of the AMMT program and will be further integrated into the LPBF 625 fabrication and qualification.

4. LOW-CHROMIUM MOLTEN SALT–COMPATIBLE ALLOYS

The previous report highlighted low-Cr Hastelloy N and Haynes 244 as the two key Ni-based alloy candidates for components requiring compatibility with molten salt at $T > 700$°C [8]. Although wrought Hastelloy N is a well-known alloy designed for molten salt applications [21] and has a large, relevant database already generated, alloy 244 is a more recent alloy with limited available data, but as shown in Figure 6, the creep properties of the alloy are drastically superior to the creep properties of Hastelloy N. To help with alloy selection, INL initiated the compatibility evaluation of alloy 244 in molten salts, and ORNL focused on the alloy printability using single-track experiments on wrought Hastelloy N and 244. A broad range of printing parameters was considered, and Figure 14 shows that none of the laser printing conditions led to the formation of any cracks. Because initial experiments carried out by INL indicated that the compatibilities of alloy 244 and Hastelloy N with molten fluoride and chloride salts are similar, alloy 244 seems to be a very promising alloy for LPBF components designed for molten salt reactors. Alloy 244 powder will be purchased to assess the alloy printability in FY 2025.

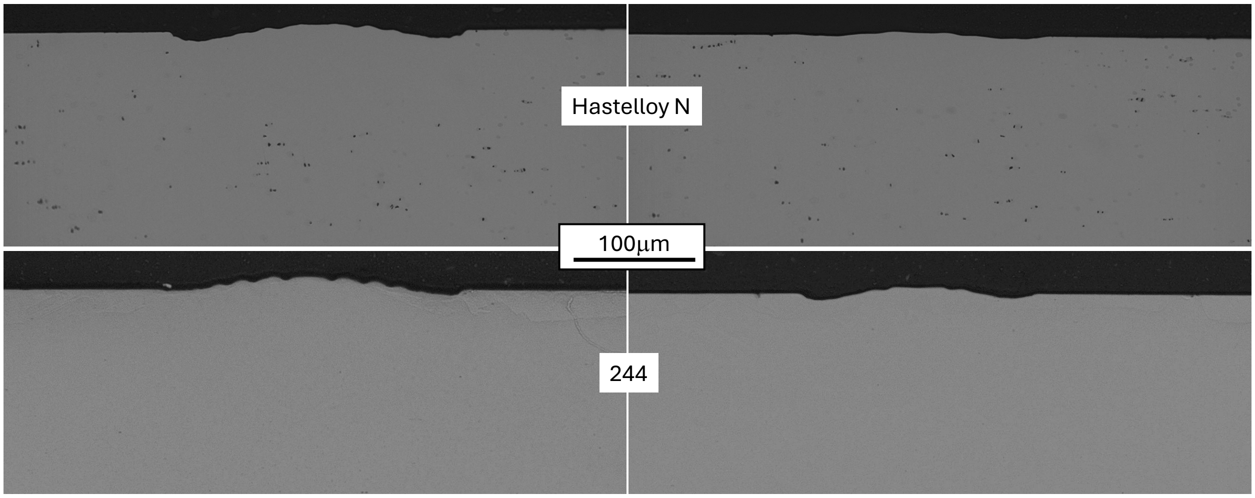

Figure 14. Micrographs highlighting the absence of crack at the surface of single-track experiments on alloy Hastelloy N and 244.

5. CONCLUSION

To select Ni-based alloys relevant to the AMMT program and the NE industry, work was performed on low-Co 718 alloy; high-temperature, high-strength 617, 230, 625, and 282 alloys; and low-Cr molten salt–compatible Hastelloy N and 244 alloys. The high creep strength of the LPBF 718 alloy in the annealed and as-printed conditions was attributed to the formation of γ' and γ'' precipitates. These precipitates can form during printing after heat treatment or during creep testing at 600°C–650°C. Formation of brittle phases at grain boundaries resulted in low ductility for all the creep tested specimens.

Printing of crack-free 617 and 230 by LPBF could not be achieved because hot tearing and composition change would likely be needed. Although alloy 230 exhibited great room-temperature tensile properties, along the BD with very high yield strength, ductility was significantly reduced perpendicular to the BD because of the presence of cracks. As expected, the fabrication of crack-free LPBF 625 using similar printing parameters was achieved, highlighting the excellent printability of the alloy. The growing interest in alloy 625 from the NE community, its satisfactory high-temperature strength and corrosion resistance, and the excellent alloy printability make LPBF 625 an exciting alloy for the AMMT program, and work will continue in FY 2025. The γ'-strengthened 282 alloy was fabricated by LPBF and creep tested at 750°C. Flaws did not affect the alloy's secondary creep rates but likely played a role in the low ductility and slightly reduced lifetimes observed for LPBF 282 specimens. XCT scans were used to establish a correlation between specimen flaws and creep properties, and ongoing analysis aims at establishing the effect of each flaw on the alloy's creep deformation. A similar approach will be implemented for both the creep and fatigue behavior of the LPBF 625 alloy. Finally, single-track experiments conducted on wrought Hastelloy N and alloy 244 did not reveal any cracking susceptibility for any of the alloys. The very high strength of alloy 244 at a high temperature might open new opportunities for the fabrication of molten salt reactor components, and the printability of the alloy will be further explored.

6. REFERENCES

1. I. Gibson, D. Rosen, B. Stucker, M. Khorasani, *Additive Manufacturing Technologies*, Vol. 17 (Springer, 2021).
2. B. R. Betzler, B. J. Ade, P. K. Jain, A. J. Wysocki, P. C. Chesser, W. M. Kirkland, M. S. Cetiner, A. Bergeron, F. Heidet, and K. A. Terrani, "Conceptual Design of the Transformational Challenge Reactor," *Nuclear Science and Engineering* 196 (2022): 1399–1424.
3. J. Haley, C. Leach, B. Jordan, R. Dehoff, and V. Pacquit, "In-Situ Digital Image Correlation and Thermal Monitoring in Directed Energy Deposition Additive Manufacturing," *Optics Express* 29, no. 7 (2021): 9927–9941.
4. A. Huning. A. Smith, L. Scime, M. Russell, A. Coates, V. Paquit, and R. Dehoff, *Advancement of Certification Methods and Applications for Industrial Deployments of Components Derived from Advanced Manufacturing Technologies*, ORNL/TM-2022/2654 (Oak Ridge, Tennessee: Oak Ridge National Laboratory, 2022).
5. M. Li, D. Andersson, R. Dehoff, A. Jokisaari, I. Van Rooyen, and D. Cairns-Gallimore, *Advanced Materials and Manufacturing Technologies (AMMT), 2022 Roadmap*, ANL-23/12 (Lemont, Illinois: Argonne National Laboratory, 2022).
6. A. Ziabari, et al., *Report Outlining Computed Tomography Strategy and Microscopy Approach to Qualifying AM 316 Materials*, ORNL/TM-2023/3016 (Oak Ridge, Tennessee: Oak Ridge National Laboratory, 2023).
7. X. Zhang, S. A. Mantri, G. I. Vukovic, J. Listwan, D. Rink, and E. Listwan, *Development of Process Parameters and Post-Build Conditions for Qualification of LPBF 316 SS*, ANL-AMMT-004 (Lemont, Illinois: Argonne National Laboratory, 2023).
8. S. Dryepondt, et al., *Prioritization of Existing Reactor Materials, 2023*, ORNL/TM-2023/3108 (Oak Ridge, Tennessee: Oak Ridge National Laboratory, 2023).
9. M. Griffiths, "Chapter 9: Ni-Based Alloys for Reactor Internals and Steam Generator Applications," in *Structural Alloys for Nuclear Energy Applications*, ed. G. R. Odette and S. J. Zinkle (Boston, Massachusetts: Elsevier, 2019).
10. S. Taller and T. Austin, "Using Post-Processing Heat Treatments to Elucidate Precipitate Strengthening of Additively Manufactured Superalloy 718," *Additive Manufacturing* 60 (2022): 103280.

11. S. Taller, A. Le Coq, C. Massey, J. Werden, M. Lynch, and K. Linton, *Report on Evolution of Inconel 718 Following HFIR Irradiation*, ORNL/TM-2022/2600 (Oak Ridge, Tennessee: Oak Ridge National Laboratory, 2022).
12. R. Wright, *Draft ASME Boiler and Pressure Vessel Code Cases and Technical Bases for Use of Alloy 617 for Constructions of Nuclear Component Under Section III, Division 5*, INL/EXT-15-36305 Revision 2 (Idaho Falls, Idaho: Idaho National Laboratory, 2021).
13. T. Hassel1 and T. Carstensen, "Properties and Anisotropy Behaviour of a Nickel Base Alloy Material Produced by Robot-Based Wire and Arc Additive Manufacturing," *Welding in the World* 64 (2020): 1921–1931.
14. B. Avinash , K. Manikanda Subramanian, and V. Rajkumar, "Microstructure, Mechanical Properties and Corrosion Behavior of Inconel 617 Superalloy Fabricated by Wire Arc Additive Manufacturing," *Journal of Materials Engineering and Performance* 32 (2023): 6270–6280.
15. "HAYNES 230 Alloy: Principal Features," Haynes International, https://haynesintl.com/en/datasheet/haynes-230-alloy/.
16. K. Momeni, "Sensitivity of Laser Powder Bed Fusion Additive Manufactured HAYNES230 to Composition and Print Parameters," *Journal of Materials Research and Technology* 15 (2021): 6453–6463.
17. Y. Zhao, Z. Ma, L. Yu, and Y. Liu, "New Alloy Design Approach to Inhibiting Hot Cracking in Laser Additive Manufactured Nickel-Based Superalloys," *Acta Materialia* 247 (2023): 118736.
18. X. Liu, R. Hu, X. Luo, C. Yang, and X. Gao, "A High-Strength Ni–Cr–W Based Superalloy Prepared by Laser Powder Bed Fusion: Printability, Microstructure and Tensile Properties," *Materials Science and Engineering A* 853 (2022): 143744.
19. T. M. Smith, "A 3D Printable Alloy Designed for Extreme Environments," *Nature* 617 (2023): 513–517.
20. C. Magnin, Z. Islam, M. Elbakhshwan, A. Brittan, D. J. Thoma, and M. H.Anderson, "The Performance of Additively Manufactured Haynes 282 in Supercritical CO_2," *Materials Science and Engineering A* 841 (2022): 143007.
21. R. W. Swindeman, *The Mechanical Properties of INOR-8*, ORNL-2780 (Oak Ridge, Tennessee: Oak Ridge National Laboratory, 1961).
22. "Haynes 244 Alloy," Haynes International Corporation, 2022.
23. S. Sanchez, P. Smith, Z. Xu, G. Gaspard, C. J. Hyde, W. W. Wits, I.A. Ashcroft, H. Chen, and A. T. Clare, "Powder Bed Fusion of Nickel-Based Superalloys: A Review," *International Journal of Machine Tools and Manufacture* 165 (2021): 103729.
24. X. Xie, J. Dong, G. Wang, and W. You, "The Effect of Nb, Ti, Al on Precipitation and Strengthening Behavior of 718 Type Superalloys," in *Superalloys 718, 625, 706 and Derivatives 2005*, ed. E. A. Loria (TMS [The Minerals, Metals and Materials Society], 2005).
25. "Inconel 625," Special Metals Corporation, 2013.
26. X. Liu, R. Hu, X. Luo, C. Yang, and X. Gao, "A High-Strength Ni–Cr–W Based Superalloy Prepared By Laser Powder Bed Fusion: Printability, Microstructure and Tensile Properties," *Materials Science and Engineering A* 853 (2022): 143744.
27. N. J. Harrison, I. Todd, and K. Mumtaz, "Reduction of Micro-Cracking in Nickel Superalloys Processed by Selective Laser Melting: A Fundamental Alloy Design Approach," *Acta Materialia* (2015): 59–68.
28. G. Marchese, G. Basile, E. Bassini, A. Aversa, M. Lombardi, D. Ugues, P. Fino, and S. Biamino, "Study of the Microstructure and Cracking Mechanisms of Hastelloy X Produced by Laser Powder Bed Fusion," *Materials* 11, no. 106 (2018).
29. D. Tomus, et al., "Controlling the Microstructure of Hastelloy-X Components Manufactured by Selective Laser Melting," *Physics Procedia* 41 (2013): 816–820.
30. Q. Han, Y. Gu, R. Setchi, F. Lacan, R. Johnston, S. L. Evans, and S. Yang, "Additive Manufacturing of High-Strength Crack-Free Ni-Based Hastelloy X Superalloy," *Additive Manufacturing* 30 (2019): 100919.

31. A. Ziabari, et al. "Enabling Rapid X-Ray CT Characterization for Additive Manufacturing Using CAD Models and Deep Learning-Based Reconstruction," *npj Computational Materials* 9, no. 91 (2023).
32. ASTM E139 – 11, Standard Test Methods for Conducting Creep, Creep-Rupture, and Stress-Rupture Tests of Metallic Materials (2018).
33. B. A. Pint, H. Wang, C. S. Hawkins, and K. A. Unocic, *Technical Qualification of New Materials for High Efficiency Coal-Fired Boilers and Other Advanced FE Concepts: Haynes 282 ASME Boiler and Pressure Vessel Code Case*, ORNL/TM-2020/1548 (Oak Ridge, Tennessee: Oak Ridge National Laboratory, 2020).
34. L. M. Pike, "Development of a Fabricable Gamma-Prime (γ′) Strengthened Superalloy," in *Superalloys*, ed. R. C. Reed, K. A. Green, P. Caron, T. P. Gabb, M. G. Fahrmann, E. S. Huron, and S. A. Woodard, 191–200 (TMS [The Minerals, Metals and Materials Society], 2008.